

## Few-layers 2D O–MoS<sub>2</sub> TFN nanofiltration membranes for future desalination

Shishi Yang<sup>a,b</sup>, Qinliang Jiang<sup>a,b</sup>, Kaisong Zhang<sup>a,\*</sup>

<sup>a</sup> Key Laboratory of Urban Pollutant Conversion, Institute of Urban Environment, Chinese Academy of Sciences, Xiamen, 361021, PR China

<sup>b</sup> University of Chinese Academy of Sciences, Beijing, 100049, PR China

### ARTICLE INFO

#### Keywords:

O–MoS<sub>2</sub>  
Nanofiltration membrane  
Interfacial polymerization  
Desalination  
Antifouling

### ABSTRACT

Advanced membranes with high water flux, excellent salt selectivity as well as superior fouling resistance are highly demanded in water desalination and water treatment. Herein, a new nanocomposite nanofiltration (NF) membrane was reported by introducing the two-dimensional (2D) oxidized molybdenum disulfide (O–MoS<sub>2</sub>) into the polyamide selective layer. O–MoS<sub>2</sub> with high hydrophilicity and strong electronegativity was synthesized by the oxidation and exfoliation process. The nanocomposite membrane was successfully prepared through interfacial polymerization with the incorporation of O–MoS<sub>2</sub> into organic phase. O–MoS<sub>2</sub> was successfully embedded in the membranes as visualized by SEM and TEM characterizations. The hydrophilicity and electronegativity of the nanocomposite membranes were improved. Compared with the pristine membrane, the performance of the membrane was best when the concentration of O–MoS<sub>2</sub> was 0.010 wt/v%. Consequently, the Na<sub>2</sub>SO<sub>4</sub> rejection increased to 97.9%, and the water flux was 2.5 times higher. In addition, the membrane displayed excellent antifouling properties. The results showed that O–MoS<sub>2</sub> as an excellent 2D modifier would bring more breakthrough improvements in the field of membrane separation.

### 1. Introduction

Membrane desalination as an advanced separation technology has been found promising in addressing water purification due to its simple operation and high efficiency, especially nanofiltration (NF) membrane can operate at lower pressures and have higher permeability compared to reverse osmosis (RO) [1,2]. However, traditional thin film composite (TFC) NF membranes are usually restricted by the “trade-off” phenomenon between flux and rejection in industrial application [3–6], as well as the inevitable membrane fouling problem which causes significant reduction in flux [7,8]. To decrease the energy consumption, preparing membranes with higher water flux, superior salt rejection and excellent fouling resistance are critically desired.

Many studies have focused on improving the membrane permeation by incorporating nanomaterials into the selective skin layer to fabricate thin film nanocomposite (TFN) membranes. Inorganic materials, such as zeolite, silica (SiO<sub>2</sub>), titanium dioxide (TiO<sub>2</sub>) and some two-dimensional (2D) materials such as boron nitride (BN) and graphene oxide (GO) are widespread used for membrane fabrication, unfortunately, often lead to the deteriorating of selectivity while improving the permeation [9–18]. In addition, the introduction of porous nanomaterials such as

metal-organic framework (MOF), zeolitic imidazolate framework (ZIF), and covalent organic framework (COF) into the membrane can provide more water channels but also give rise to the non-selective voids created when carrying out interfacial polymerization [19–21]. Meanwhile, the surface properties of the membrane have a great influence on the antifouling performance, it is easier with antifouling properties by modifying the surface of the TFC membrane via grafting or coating to make it more hydrophilic [22]. Grafting of polyethylene glycol and coating with dopamine or zwitterionic can improve the hydrophilicity of the membrane surface, while the flux of the membrane will decrease as the thickness of the separation layer increases [23–25]. In addition, enhancing the charge property of the membrane surface and utilizing electrostatic repulsion can also effectively improve the antifouling performance [26–28]. In general, the study of hydrophilic, charged nanomaterials may have a great influence on improving the membrane permeability and selectivity, as well as antifouling performance.

Recently, novel 2D molybdenum disulfide (MoS<sub>2</sub>) nanosheets were found promising in membrane fabrication due to the atomic thickness, unique physicochemical properties as well as their ease of preparation [26,29–32]. The researchers found that the flux of MoS<sub>2</sub> membrane was higher than graphene membrane prepared under the same conditions

\* Corresponding author.

E-mail address: [kszhang@iue.ac.cn](mailto:kszhang@iue.ac.cn) (K. Zhang).

<https://doi.org/10.1016/j.memsci.2020.118052>

Received 6 January 2020; Received in revised form 10 March 2020; Accepted 11 March 2020

Available online 13 March 2020

0376-7388/© 2020 Elsevier B.V. All rights reserved.

according to the molecular dynamics simulation [33]. In our previous work [26,34], it was discovered that the exfoliated few-layers MoS<sub>2</sub> with negative charged, and had good hydrophilicity at the same time, incorporation into the polyamide (PA) layer by interfacial polymerization could simultaneously improve the permeability and selectivity of the NF and RO membranes. Especially in the MoS<sub>2</sub>-TFN NF modification, the water flux was 2.3 times more than the TFC membrane without sacrificing the salt rejection. Inspired by the oxidization of graphene nanosheets using Hummers' method, we hypothesize that this similar method of oxidation and exfoliation can endow MoS<sub>2</sub> to be more hydrophilic and electronegative [35]. By using the obtained oxidized molybdenum disulfide (O-MoS<sub>2</sub>) as nanofiller, the hydrophilicity, flux and antifouling performance of the TFN membrane are expected to be greatly improved.

In this work, O-MoS<sub>2</sub> with high hydrophilicity and electronegativity was prepared by exfoliation and oxidation through Hummers' method. The TFN NF membranes were successfully prepared by adding the O-MoS<sub>2</sub> in organic phase with different concentrations via interfacial polymerization. Scanning electron microscope (SEM) and transmission electron microscope (TEM) were utilized to confirm the successful incorporation of O-MoS<sub>2</sub> in the TFN membrane. Compared to the MoS<sub>2</sub>-TFN membrane prepared in our previous work, the O-MoS<sub>2</sub> TFN membrane has an unprecedented enhancement in permeability and selectivity due to the introduction of O-MoS<sub>2</sub>, and has excellent antifouling performance. The successful application of 2D O-MoS<sub>2</sub> nanosheets materials in NF membranes has opened up a new way for water desalination.

## 2. Experiment

### 2.1. Materials

The support layer of the NF membrane was a laboratory-made polysulfone (PSf) ultrafiltration (UF) membrane, with a flux of 293 L m<sup>-2</sup> h<sup>-1</sup> (1.0 bar) and rejection of bovine serum albumin (BSA) was 97.8%. Piperazine (PIP, 99%), 1,3,5-benzenetricarbonyl trichloride (TMC, 98%), triethylamine (TEA, 99%), (±)-camphor-10-sulfonic acid (CSA, 99%), Na<sub>2</sub>SO<sub>4</sub> (99%), MgSO<sub>4</sub>, MgCl<sub>2</sub> (99.9%), NaCl (99.5%), BSA (96%) and KCl (99.99%) were purchased from Aladdin. MoS<sub>2</sub> was supplied from Sigma-Aldrich. H<sub>2</sub>SO<sub>4</sub> (98%), NaNO<sub>3</sub>, KMnO<sub>4</sub>, HCl, H<sub>2</sub>O<sub>2</sub> (30%), sodium dodecyl sulfate (SDS), polyethylene glycol (PEG) and n-hexane were obtained by Sinopharm Chemical Reagent Co., Ltd. Deionized (DI) water was used throughout the experiment, the temperature was about 25 ± 2 °C, and the conductivity was about 1.0 ± 0.3 μS/cm.

### 2.2. Preparation of O-MoS<sub>2</sub>

The synthesis of O-MoS<sub>2</sub> was referred to the Hummers' method as reported elsewhere [35]. In brief, 3.0 g MoS<sub>2</sub> powder mixed with 50 mL 98% H<sub>2</sub>SO<sub>4</sub> and 1.0 g NaNO<sub>3</sub> with stirring at room temperature for 12 h, followed by adding 6.0 g KMnO<sub>4</sub> slowly under the condition of ice bath (0 °C). After that, the solution was stirred in the oil bath (35 °C) for 3 h to get the brown liquid, then put it back in the ice bath and added 100 mL DI water in the solution to cool to room temperature. Then, 8.0 mL 30% H<sub>2</sub>O<sub>2</sub> was added until the solution became yellow. The hot mixture solution was filtrated through 0.1 μm polytetrafluoroethylene (PTFE) microfiltration (MF) membrane and washed with 250 mL 10% HCl to remove excess metal ions. Ultimately, the few layered O-MoS<sub>2</sub> nanomaterial was obtained by exfoliation for 3 h and then drying in the oven at 60 °C for 24 h.

### 2.3. Preparation of O-MoS<sub>2</sub> NF membrane

The preparation methods of PSf UF membrane as reported in the previous work [36], the specific method for preparing O-MoS<sub>2</sub> TFN membrane was as follows: the PSf UF membrane was immersed in DI

water for 4 h for future use, the aqueous phase consisted of 92.28 wt% DI water, 3.00 wt% CSA, 3.00 wt% TEA, 0.12 wt% SDS and 1.60 wt% PIP, the organic phase consisted of 0.35 wt/v% TMC in n-hexane and different amount (0.000, 0.004, 0.007, 0.008, 0.009, 0.010, 0.011 and 0.012 wt/v%) of O-MoS<sub>2</sub>. First, the aqueous phase solution was deposited on the PSf UF membrane for 45 s, followed immersion in TMC organic phase for 20 s after removal of the residual aqueous phase solution, and then the membrane was placed in an oven at 60 °C for 2 min. Finally, the membrane was stored in DI water for later use. The content of O-MoS<sub>2</sub> at 0.000, 0.004, 0.007, 0.008, 0.009, 0.010, 0.011 and 0.012 wt/v% were named as M0, M1, M2, M3, M4, M5, M6 and M7, respectively. In the characterization of the membranes, 5 membranes were selected (M0, M1, M3, M5, M7) with increasing concentration of O-MoS<sub>2</sub> for measurement. The diagram of interfacial polymerization is shown in Fig. 1.

### 2.4. Characterization of O-MoS<sub>2</sub>

The lamellar structure of MoS<sub>2</sub> and O-MoS<sub>2</sub> was characterized by transmission electron microscope (TEM, JEM-2100, JEOL, Japan) under 200 kV. The hydrophilicity, crystal structure and charge of the MoS<sub>2</sub> and O-MoS<sub>2</sub> were measured using contact angle analyzer (DSA100, KRUSS, German), X-ray diffraction (XRD, X'Pert Pro, PANalytical, Netherlands) and zeta potential (Zeta PALS, Malvern, Britain), respectively. The contact angles of MoS<sub>2</sub> and O-MoS<sub>2</sub> were tested with DI water and methanol, respectively. According to the Owens-Wendt equation below (Eqs. (1) and (2) [37,38]), the surface free energy change of MoS<sub>2</sub> and O-MoS<sub>2</sub> was calculated. While for the XRD test, the operating voltage and current conditions were 40 kV and 40 mA. For the charge measurement, the pH values ranged from 3 to 10. The thickness and morphology of O-MoS<sub>2</sub> nanosheets were observed by atomic force microscopy (AFM, Dimension 3100, Bruker, USA). The atomic composition of MoS<sub>2</sub> and O-MoS<sub>2</sub> was studied by X-ray photoelectron spectroscopy (XPS, ESCALAB 250XI, Thermo, USA). The chemical structure of bulk MoS<sub>2</sub> and prepared O-MoS<sub>2</sub> was observed by Fourier transform infrared spectroscopy (FTIR, Nicolet iS10, Thermo, USA), range of wavenumber was 400–4000 cm<sup>-1</sup>.

$$(1 + \cos \theta)\gamma_{lv} = 2\sqrt{\gamma_S^D \times \gamma_L^D} + 2\sqrt{\gamma_S^P \times \gamma_L^P} \quad (1)$$

$$\gamma_S = \gamma_S^D + \gamma_S^P \quad (2)$$

Where  $\theta$  was the contact angle of water or methanol,  $\gamma_{lv}$  was the surface tension of the liquid, the  $\gamma_L^D$  and  $\gamma_L^P$  were the surface tension of the liquid dispersion and polarity parts, respectively.  $\gamma_S^D$  and  $\gamma_S^P$  were similar to  $\gamma_L^D$  and  $\gamma_L^P$ .  $\gamma_S$  represented the total surface free energy of MoS<sub>2</sub> and O-MoS<sub>2</sub>.

### 2.5. Characterization of O-MoS<sub>2</sub> NF membrane

The surface and cross-sectional morphologies of the membranes were observed by field-emission scanning electron microscope (SEM, S-4800, HITACHI, Japan), the operating voltage and current conditions were 5 kV and 10 μA. Transmission electron microscope (TEM, H-7650, HITACHI, Japan) was used to analyse the cross-sectional of the control and the O-MoS<sub>2</sub> NF membranes for in depth study, the operating voltage and current conditions were 100 kV and 20 μA. The location of O-MoS<sub>2</sub> nanosheets material on O-MoS<sub>2</sub> NF membrane were characterized by energy dispersive X-ray spectrometer (EDX, Oxford 6587, HITACHI, Japan), the operating voltage and current conditions were 20 kV and 15 μA. The surface roughness of membranes was examined by atomic force microscopy (AFM, Dimension 3100, Bruker, USA). The hydrophilicity of membranes was evaluated by contact angle analyzer (DSA100, KRUSS, German). The surface charge of the membranes was tested by zeta potential (SurPASS 3, Anton Paar, Australia), the background electrolyte solution was 1 mM KCl, the pH was adjusted by the 0.05 mol/L HCl and

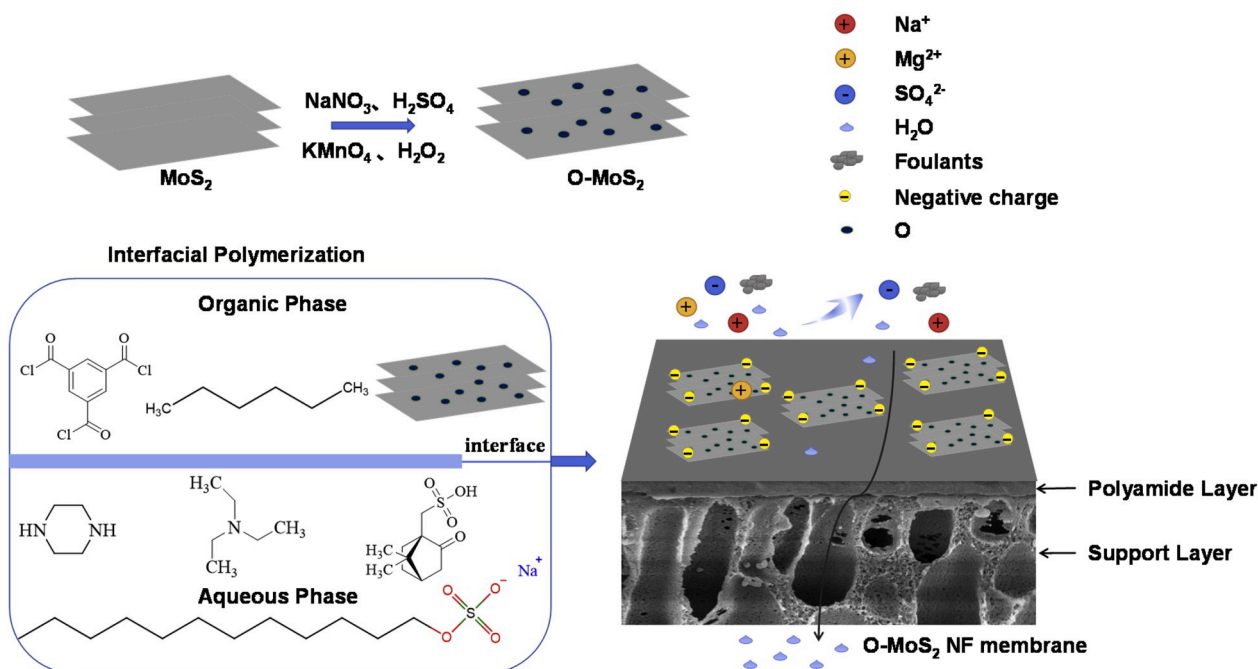


Fig. 1. Diagram of interfacial polymerization.

NaOH, the gap height was about 100  $\mu\text{m}$ . The atomic composition of membranes was determined by X-ray photoelectron spectroscopy (XPS, Axis Supra, Kratos, Britain). PEG of different molecular weights (200, 300, 400, 600 and 1000 Da) were filtered through the NF membranes, and the molecular weight cut-off (MWCO) was measured by Toc-Vcph analyzer (Shimadzu, Japan).

## 2.6. Performance of O-MoS<sub>2</sub> NF membrane

The separation performance of the TFN membranes was tested by a dead-end filter cell. The pressure was applied with nitrogen at 3.5 bar, and the obtained weighed data from the analytical balance were recorded in the computer. The feed solutions were prepared with Na<sub>2</sub>SO<sub>4</sub>, MgSO<sub>4</sub>, MgCl<sub>2</sub> and NaCl at 2000 ppm. Each membrane was compacted for 30 min and then tested, the results were recorded by the computer and calculated according to the following formula.

The water flux was measured by the total volume of the permeable solution within a fixed time and effective area using Eq. (3):

$$J_w = \frac{Q}{At} \quad (3)$$

where  $J_w$  was the water flux ( $\text{L m}^{-2} \text{h}^{-1}$ ),  $Q$  was the total volume of the permeable solution (L) during the  $t$  (h) period, and  $A$  was the effective area of the testing membrane ( $\text{m}^2$ ).

A portable conductivity meter (sensION + EC5, HACH) was used to determine the conductivity of the feed and permeate solutions, and then the separation performance was calculated by Eq. (4):

$$R(\%) = \left(1 - \frac{C_p}{C_f}\right) \times 100 \quad (4)$$

Where  $C_p$  and  $C_f$  was the salt concentration of permeate and feed solutions, respectively.

## 2.7. Pore size and pore size distribution of O-MoS<sub>2</sub> NF membrane

The NF membranes were tested with 1000 ppm PEG at different molecular weights, similar to salt filtration, the calculation method of PEG separation performance was the same as Eq. (4). The rejection of

90% and 50% corresponded to the MWCO and mean effective pore diameter ( $\mu_p$ ) of the membrane, respectively. The pore size and pore size distribution of the membrane were analyzed by Eqs. (5)–(7) [39,40].

$$a = 16.73 \times 10^{-10} \times M_{PEG}^{0.557} \quad (5)$$

$$d_s = 2 \times a \times 10^7 \quad (6)$$

$$\frac{dR(d_p)}{dd_p} = \frac{1}{d_p \ln \sigma_p \sqrt{2\pi}} \exp \left[ -\frac{(\ln d_p - \ln \mu_p)^2}{2(\ln \sigma_p)^2} \right] \quad (7)$$

where  $a$  (cm) and  $d_s$  (nm) corresponded to the Stokes radius and diameter of the PEG, respectively. Under the condition that only the sieving effect between PEG and membrane pores was considered, the Stokes diameter ( $\mu_s$ ) at PEG rejection of 50% approximately equaled the mean effective pore diameter ( $\mu_p$ ) of the membrane. The Stokes diameter ratio with PEG rejection at 84.13% and 50% was defined as the geometric standard deviation ( $\sigma_g$ ), which was roughly equivalent to the geometric standard deviation ( $\sigma_p$ ).

## 2.8. Antifouling performance of O-MoS<sub>2</sub> NF membrane

The membrane used for the antifouling test was filtered with DI water at room temperature and 3.5 bar for 60 min until the water flux reached a stable value, defined it as initial permeate flux ( $J_0$ ). The membrane after 90 min of 500 ppm BSA filtration was repeatedly rinsed with DI water to remove residual contaminants on the surface, and finally filtered with DI water for 90 min to obtain a stable water flux ( $J$ ). The flux recovery rate (FRR) of the membrane by Eq. (8):

$$FRR = (J / J_0) \times 100\% \quad (8)$$

## 3. Results and discussion

### 3.1. Physicochemical characterization of MoS<sub>2</sub> and O-MoS<sub>2</sub>

As shown in Fig. 2a, the bulk MoS<sub>2</sub> crystals presented a multi-layer structure due to van der Waals force between layers. However, it could be seen in Fig. 2b due to the strong external force of ultrasound in

the process and the intensity oxidation effect, the MoS<sub>2</sub> layers were effectively exfoliated and shattered [41]. Especially in Fig. 2c-d, the number of O-MoS<sub>2</sub> nanosheets could be observed to be six.

As shown in Fig. 3, whether it was DI water or methanol, O-MoS<sub>2</sub> showed a smaller contact angle. According to the relevant parameters of Table S1, the surface free energy of MoS<sub>2</sub> and O-MoS<sub>2</sub> was calculated, the results were shown in Table S2. It could be found that the surface polarity and surface free energy of the synthesized O-MoS<sub>2</sub> increased, higher surface free energy meant better hydrophilicity, perhaps due to the formation of hydrophilic oxygen-containing functional groups [42]. The increased hydrophilicity of MoS<sub>2</sub> nanosheets was expected to endow the nanocomposite membrane surface with enhanced hydrophilicity which promoted the water permeability.

The diffraction angle of O-MoS<sub>2</sub> ( $2\theta = 14.2^\circ$ ) in X-ray diffraction (XRD) pattern was decreased compared with the pristine MoS<sub>2</sub> crystals ( $2\theta = 14.5^\circ$ ) in Fig. 4a. According to Bragg's law  $n\lambda = 2d\sin\theta$ , the O-MoS<sub>2</sub> layer spacing ( $d = 0.62$  nm) tended to increase due to the strong oxidation process compared to the MoS<sub>2</sub> crystal ( $d = 0.60$  nm). In addition, the O-MoS<sub>2</sub> nanosheets showed a more negative charged property in a wide pH range as was confirmed from the zeta potential characterization in Fig. 4b. Interestingly, at pH of 7, the zeta potential of the O-MoS<sub>2</sub> nanosheets was as high as -53.5 mV. In the process of oxidation and exfoliation, the lateral size and layers of nanosheets material further reduced, and more sulfur (S) atoms were exposed at the edge of the nanosheets. When exposed to a strong oxidant, the S edge sites were easily oxidized, resulting in more negative charge on O-MoS<sub>2</sub> [43,44]. Furthermore, the thickness of the O-MoS<sub>2</sub> nanosheets was characterized by atomic force microscope (AFM), three points were randomly selected, and the results were shown in Fig. 4c-f. The size of the O-MoS<sub>2</sub> nanosheets was around several hundred nanometers, since the thickness of the single-layer O-MoS<sub>2</sub> was about 0.62 nm, the

synthesized O-MoS<sub>2</sub> in this work was approximately 3–7 layers, which was few-layers structure.

X-ray photoelectron spectroscopy (XPS) was used to analyse the Mo, S, O element content and the different valence states in the MoS<sub>2</sub> and O-MoS<sub>2</sub>, the results were shown in Fig. 5 [45]. As shown in Table 1, it could be found that there existed a trace of oxygen (2.3%) in MoS<sub>2</sub>. This could be probably originated from the air or the water vapor adsorbed on the surface of MoS<sub>2</sub>. In contrast, a high content of oxygen (15.5%) was found for O-MoS<sub>2</sub>, indicating the successfully oxidation of the nanomaterials. The underlying oxidation process could be confirmed from the O 1s spectra of the O-MoS<sub>2</sub>. A new peak at 531.0 eV was found and could be ascribing to the Mo–O bond. Meanwhile, the high-resolution XPS spectra of Mo 3d and S 2p in O-MoS<sub>2</sub> shifted to the high energy region after oxidation and exfoliation. This may have been caused by the decrease in electron cloud density during oxidation [46].

Fig. 6 showed the Fourier transform infrared spectroscopy (FTIR) spectra of the MoS<sub>2</sub> and the O-MoS<sub>2</sub>. After oxidation and exfoliation, O-MoS<sub>2</sub> was observed with an absorption peak of S=O at 1191 cm<sup>-1</sup> [35]. In addition, both MoS<sub>2</sub> and O-MoS<sub>2</sub> had a absorption peak at 1611 cm<sup>-1</sup>, which may be due to the inevitable adsorption of water molecules on the nanosheets materials surface [47]. Combined with the results of XPS and FTIR, the formation of oxygen-containing groups such as Mo–O bond and S=O bond may cause the decreased diffraction angle and increased interlayer spacing [48–50]. Moreover, the expanded interlayers of O-MoS<sub>2</sub> were likely due to the intercalation of H<sub>2</sub>SO<sub>4</sub> and H<sub>2</sub>O into two S–Mo–S layers under the oxidation reaction [45,51,52].

### 3.2. Characterization of O-MoS<sub>2</sub> NF membrane

The surface and cross-sectional morphologies of membranes were observed by scanning electron microscope (SEM) under 30,000

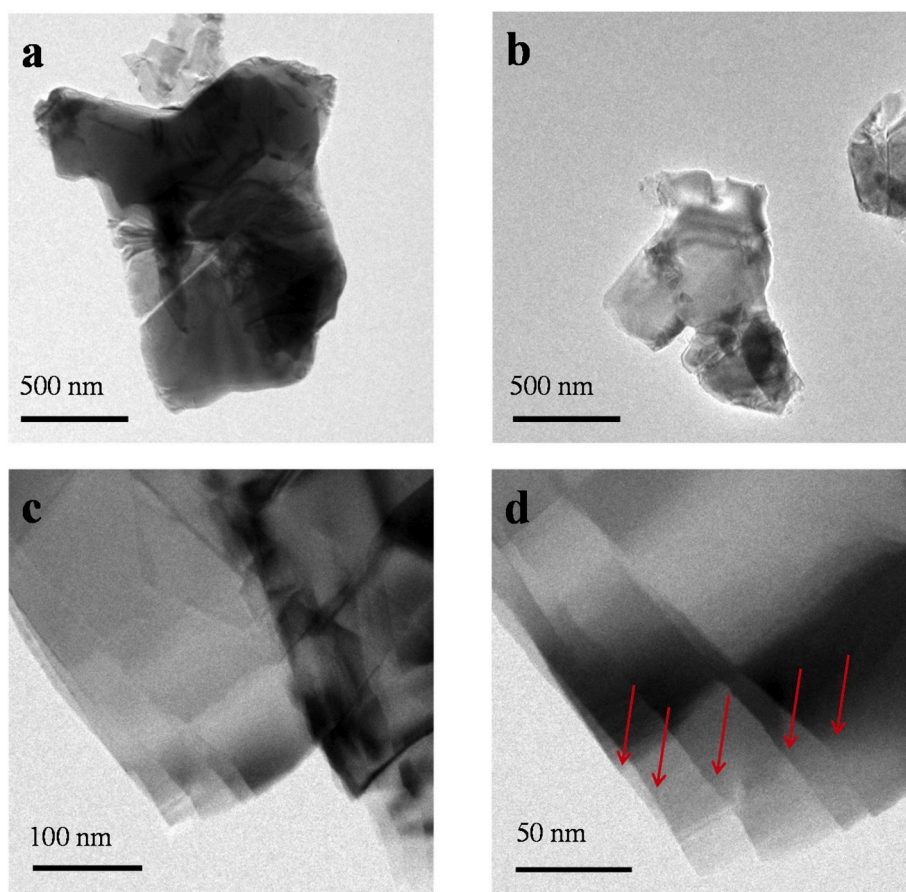


Fig. 2. TEM of (a) bulk MoS<sub>2</sub> and (b-d) O-MoS<sub>2</sub>.

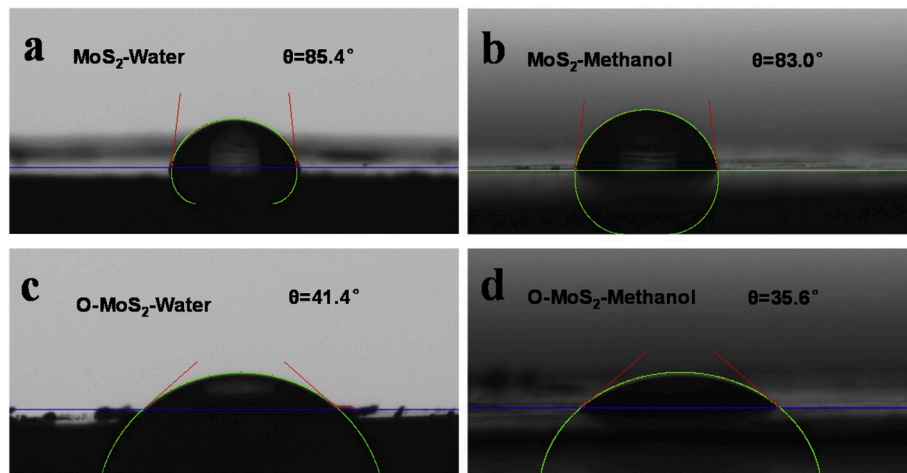


Fig. 3. Contact angle of MoS<sub>2</sub> (a,b) and O-MoS<sub>2</sub> (c,d) under water and methanol.

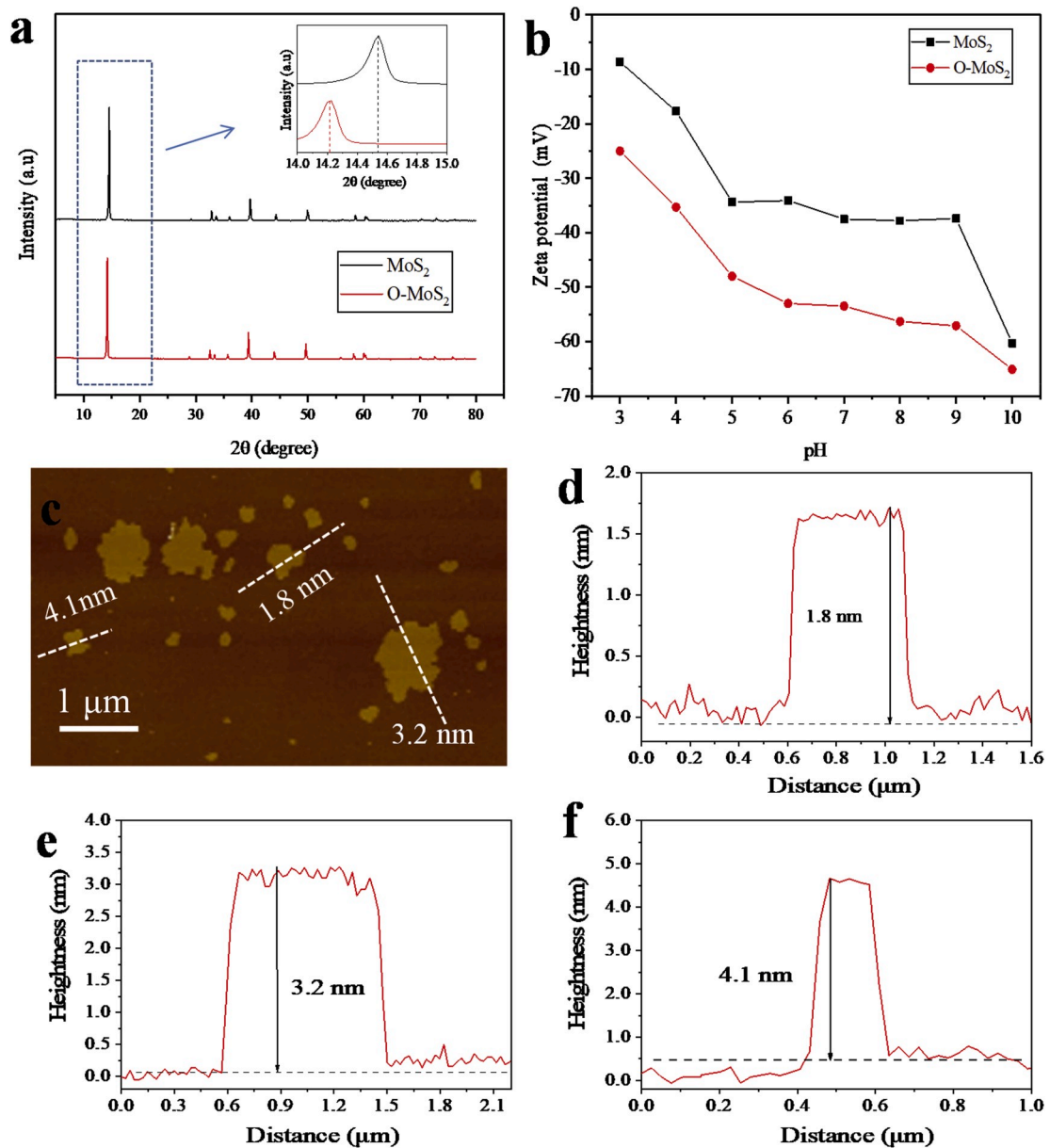
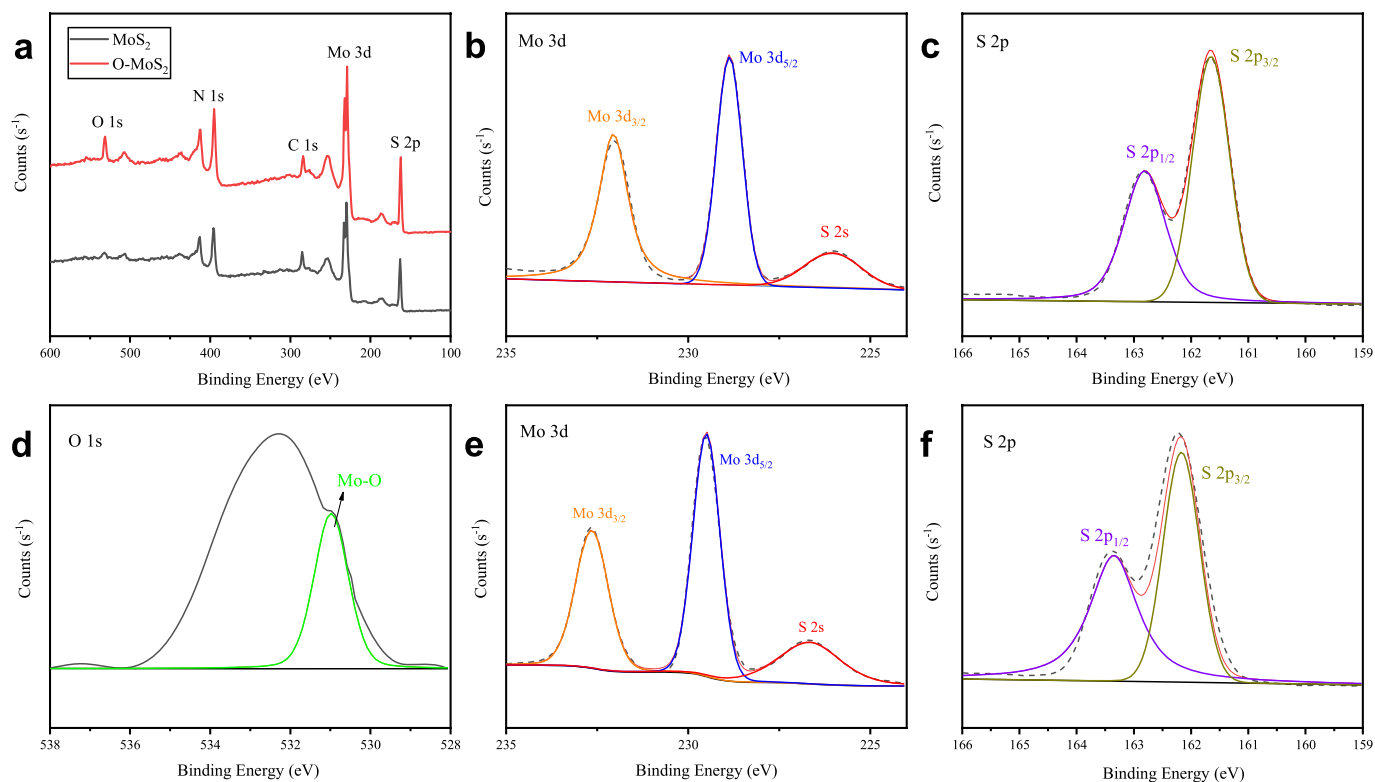


Fig. 4. XRD pattern (a) and zeta potential (b) of MoS<sub>2</sub> and O-MoS<sub>2</sub>, AFM of O-MoS<sub>2</sub> (c-f).



**Fig. 5.** XPS spectra for MoS<sub>2</sub> and O-MoS<sub>2</sub>(a), high-resolution XPS spectra of (b) Mo 3d and (c) S 2p for MoS<sub>2</sub>, (d) O 1s, (e) Mo 3d and (f) S 2p for O-MoS<sub>2</sub>.

**Table 1**

XPS analysis for the atomic composition of MoS<sub>2</sub> and O-MoS<sub>2</sub>.

| Conc./%            | S    | Mo   | O    |
|--------------------|------|------|------|
| MoS <sub>2</sub>   | 63.2 | 34.5 | 2.3  |
| O-MoS <sub>2</sub> | 52.9 | 31.6 | 15.5 |

magnifications. It could be seen in Fig. 7 that the pristine membrane surface showed a representative bubble structures with round protrusions because of the fast reaction of PIP with TMC [53]. The O-MoS<sub>2</sub> nanosheets could be observed on the modified TFN membrane surface with a random distribution, which was marked in Fig. 7 with white circle. Under the observation of SEM, O-MoS<sub>2</sub> was successfully embedded on the surface and in the cross-section PA layer of the membranes. This was similar to the morphology of the MoS<sub>2</sub>-TFN membranes observed in previous work. The cross-sectional image of MO

and M5 was observed using the transmission electron microscope (TEM) in a magnification of 20,000 to further confirm the successful incorporation of O-MoS<sub>2</sub> in the membrane selective layer. As shown in Fig. 8a, the PA layer was supported on the porous PSf substrate. Interestingly, as shown in Fig. 8b-c, the O-MoS<sub>2</sub> was found successfully embedded in the PA layer, which could be easily observed from the dark 2D nanosheets with size of hundreds of nanometers. Energy dispersive X-ray spectrometer (EDX) elemental mapping allowed further analysis of the distribution of O-MoS<sub>2</sub> nanosheets on the TFN membrane surface, the result was shown in Fig. S1.

The surface roughness of NF membranes was measured by AFM, three-dimensional (3D) scan photos were displayed in Fig. 9, in three random points with scan area of 2 μm × 2 μm for each membrane, the surface roughness parameters (average roughness: Ra, root mean-square roughness: Rq, maximum vertical distance: Rz) of membranes were summarized in Table 2. From Fig. 9 and Table 2, it could be found that as the concentration of O-MoS<sub>2</sub> increased, the surface roughness of the

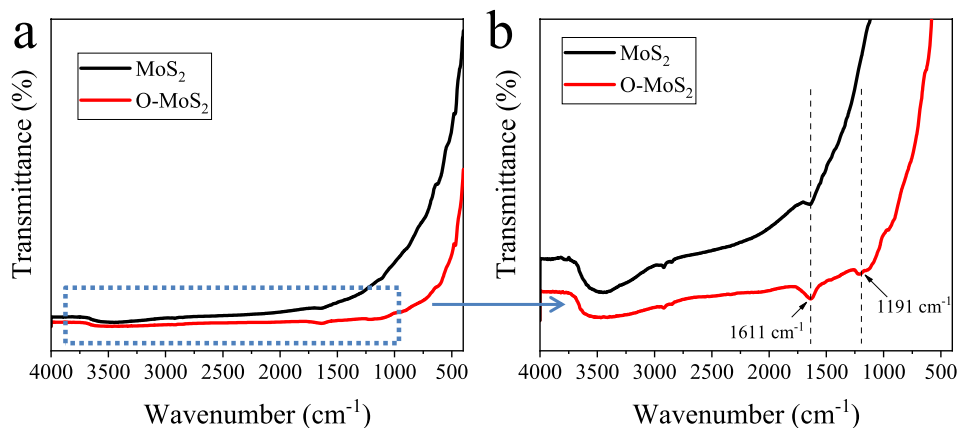


**Fig. 6.** FTIR spectra of MoS<sub>2</sub> and O-MoS<sub>2</sub>.

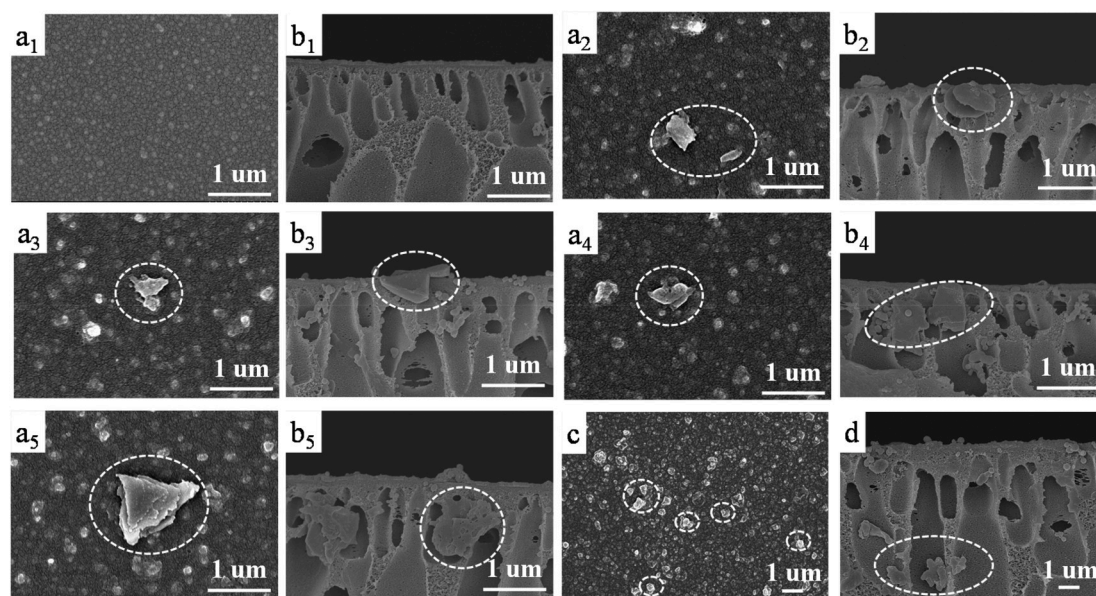


Fig. 7. SEM surface and cross-sectional morphologies of M0 (a<sub>1</sub>, b<sub>1</sub>), M1 (a<sub>2</sub>, b<sub>2</sub>), M3 (a<sub>3</sub>, b<sub>3</sub>), M5 (a<sub>4</sub>, b<sub>4</sub>), M7 (a<sub>5</sub>, b<sub>5</sub>) and MoS<sub>2</sub>-TFN membrane (c–d).

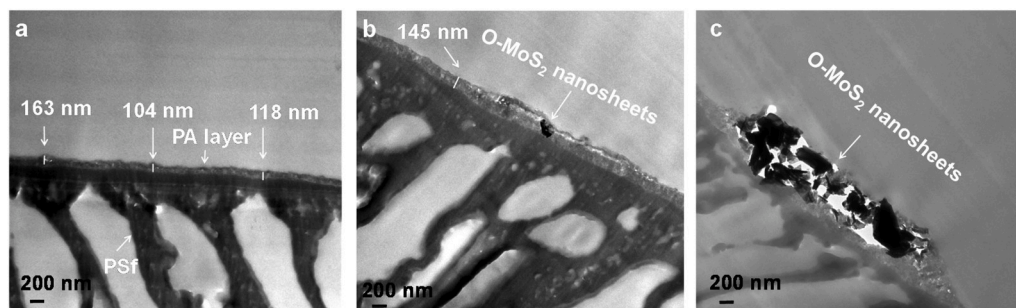


Fig. 8. TEM of (a) M0 and (b–c) M5 NF membranes.

membranes gradually increased. A rougher membrane surface meant a successful incorporation of O–MoS<sub>2</sub> nanosheets material [54,55], and could provide more contact area for water and thus enhance permeability [56–59].

To approve the effect of O–MoS<sub>2</sub> addition to the selective layer of the membranes, XPS was utilized to examine the content of the element of C, N, O, S and Mo. Subsequently, the degree of network cross-linking (DNC) of the polyamide layer was calculated based on the element content [60]. The results were shown in Table 3. With the addition of O–MoS<sub>2</sub> nanosheets, XPS detected the presence of S and Mo elements and increased. The formation of Mo–O and S=O bonds further enhanced the DNC of the TFN membranes, which played a positive role in the desalination performance of the membranes [61].

Fig. 10a displayed that the traditional TFC NF membrane prepared by PIP and TMC showed a negatively charged membrane surface at a neutral pH with a zeta potential of -19.6 mV. Interestingly, after the introduction of O–MoS<sub>2</sub>, the electronegativity of NF membranes with the O–MoS<sub>2</sub> nanosheets modification showed an improvement with the increase of the content of O–MoS<sub>2</sub>, from -19.6 mV of M0 to -35.0 mV of M5. Since NF is a separation process based on the sieving effect and Donnan effect, the surface charge properties were very important for the desalination performance of the membrane [62]. The results demonstrated that the negatively charged O–MoS<sub>2</sub> nanosheets successfully endowed the TFN membrane with more electronegativity properties, leading to an increased repulsion to negatively charged salt ions, which further improved the selectivity of the TFN membrane.

It could be found in Fig. 10b that the hydrophilic property of the

control TFC membrane surface was not ideal, and the contact angle was maintained at about 75°. With the addition of the more hydrophilic O–MoS<sub>2</sub> (water contact angle was 41.4°), the TFN membrane showed excellent hydrophilicity and the contact angle was reduced from 75° to about 41°. Since the roughness of the membrane surface was related to hydrophilicity, according to the Wenzel's law  $\cos\theta^* = r \cos\theta$ , where the  $\theta^*$  was the measured contact angle,  $\theta$  was Young angle,  $r$  was roughness factor, meant the ratio of the actual to the flat surface areas [63,64]. The  $r$  was more than 1 for rough and hydrophilic surface, the contact angle was negatively correlated with the roughness, the rougher of the membrane surface, the smaller of the contact angle, which meant the membrane was more hydrophilic [65].

### 3.3. Performance of O–MoS<sub>2</sub> NF membrane

Generally, NF membrane has a molecular weight cut-off (MWCO) between 150–1000 Da [66]. In this work, the MWCO was examined for both pristine membrane (M0) and nanocomposite membrane (M5) by molecular rejection experiment using natural charged PEG solution, the results were shown in Fig. 11a–b. The MWCO of the M0 membrane was 497 Da, and the mean effective pore diameter ( $\mu_p$ ) at the corresponding rejection of 50% was 0.65 nm. After the incorporation of O–MoS<sub>2</sub>, the MWCO of the M5 membrane was significantly reduced to 375 Da, and the corresponding  $\mu_p$  was 0.56 nm. The reduction in MWCO and membrane pore size could be attributed to the following two reasons: 1) Mo–O and S=O bonds were formed after oxidation of MoS<sub>2</sub>, which promoted the interfacial polymerization process and enhanced the

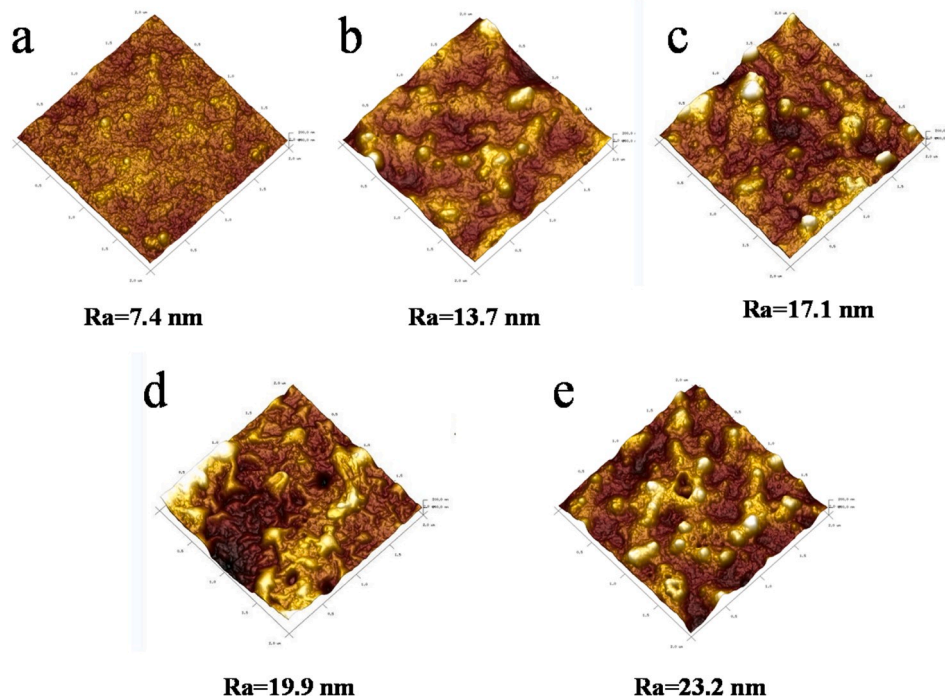


Fig. 9. AFM 3D morphologies of M0 (a), M1 (b), M3 (c), M5 (d) and M7 (e).

Table 2

Surface roughness parameters of modified membranes with different loading content of O-MoS<sub>2</sub>.

| Membrane NO. | Ra(nm)     | Rq(nm)     | Rz(nm)       |
|--------------|------------|------------|--------------|
| M0           | 7.4 ± 0.3  | 9.7 ± 0.4  | 82.5 ± 4.2   |
| M1           | 13.7 ± 0.9 | 18.1 ± 0.6 | 157.0 ± 26.5 |
| M3           | 17.1 ± 0.4 | 25.0 ± 4.4 | 207.0 ± 30.6 |
| M5           | 19.9 ± 1.8 | 26.5 ± 2.5 | 195.7 ± 32.3 |
| M7           | 23.2 ± 1.9 | 31.2 ± 1.4 | 213.0 ± 37.9 |

Table 3

The composition and degree of cross-linking of TFC and TFN membranes.

| Membranes | C (%) | N (%) | O (%) | S (%) | Mo (%) | O/N  | DNC (%) |
|-----------|-------|-------|-------|-------|--------|------|---------|
| M0        | 86.62 | 5.10  | 8.28  | –     | –      | 1.62 | 29      |
| M1        | 84.75 | 6.06  | 9.07  | 0.10  | 0.02   | 1.50 | 40      |
| M3        | 77.11 | 9.62  | 13.08 | 0.14  | 0.05   | 1.36 | 54      |
| M5        | 73.32 | 11.74 | 14.71 | 0.16  | 0.07   | 1.25 | 67      |
| M7        | 70.46 | 13.40 | 15.86 | 0.18  | 0.10   | 1.18 | 75      |

density of the membrane [34]. 2) The O-MoS<sub>2</sub> nanosheet layer partially covered the PIP-TMC crosslinked network, which will have an impact on the reduction of MWCO [61]. The pure water flux of the membranes in Fig. 11c increased with an increase of O-MoS<sub>2</sub> concentration. Significantly, the membrane with the addition of 0.010 wt/v% of O-MoS<sub>2</sub> showed the highest water flux of 27.7 L m<sup>-2</sup> h<sup>-1</sup>, which was almost 2.5 times higher than the pristine membrane (10.9 L m<sup>-2</sup> h<sup>-1</sup>). Moreover, in Fig. 11d, the four salt rejections were also improved with the addition of O-MoS<sub>2</sub>, the rejection of Na<sub>2</sub>SO<sub>4</sub> increased from 93.4% to 97.9%, MgSO<sub>4</sub> increased from 89.9% to 92.9% and MgCl<sub>2</sub> increased from 73.8% to 86.3%. Interestingly, the rejection for NaCl was enhanced remarkably from 34.7% to 65.1% at O-MoS<sub>2</sub> loading content of 0.010 wt/v%. The radius of the hydrated salts ions of Na<sup>+</sup> was 3.58 Å and Cl<sup>-</sup> was 3.32 Å [67], while the μ<sub>p</sub> of the TFN NF membrane modified by O-MoS<sub>2</sub> was 0.56 nm, and the radius was 0.28 nm. The reduction of the membrane pore size had a crucial effect on the improvement of NaCl rejection. In summary, the O-MoS<sub>2</sub> nanosheets played an important role in

improving the TFN NF membrane, the membrane separation performance was optimized when the content of O-MoS<sub>2</sub> was 0.010 wt/v%.

The raised of hydrophilicity (Fig. 10b showed) on the membranes surface was an important reason for the enhancement of membrane flux, because the hydrophilic sites on the O-MoS<sub>2</sub> nanosheets layer can generate a high affinity with water molecules through hydrogen bonds, further increasing the water flux [26]. At the same time, the increasing in surface roughness was expected to improve the contact of water molecules and membrane surface [68]. Fig. 4 showed that interlayer spacing of O-MoS<sub>2</sub> (0.62 nm) further increased compared with MoS<sub>2</sub> (0.60 nm) after oxidation, and was larger than water molecules (0.276 nm) [69]. O-MoS<sub>2</sub> with more hydrophilic and larger interlayer spacing could play a positive role in water transport, and enhanced the permeability of the membranes.

As mentioned above, the prepared O-MoS<sub>2</sub> composite NF membrane remained negative charge under a wide pH range of 3–10. For example, the nanocomposite membrane prepared from 0.010 wt/v% O-MoS<sub>2</sub> had a zeta potential of -35.0 mV at a neutral pH, which may be the reason why the salt rejection of the NF membranes improved according to the Donnan effect. The electronegativity on the membrane surface corresponded to the negative charge of the membrane, the more negative charges, the stronger the repulsive force on the anions, so that the higher the rejection [70]. Meanwhile, there was also a sieving effect in the separation mechanism of the NF membrane, and the decrease of membrane pore size had a positive effect on the salt rejection. Overall, the salt rejection was found in a sequence of: Na<sub>2</sub>SO<sub>4</sub> > MgSO<sub>4</sub> > MgCl<sub>2</sub> > NaCl, which was consistent with many reports with negatively charged NF membranes [71–74]. Within our knowledge, the rejection of Na<sub>2</sub>SO<sub>4</sub> was higher than other reported MoS<sub>2</sub> membranes [30,75,76]. The O-MoS<sub>2</sub> TFN NF membranes prepared in this work had a great improvement in salt rejection, flux and antifouling performance, it exceeded that of TFC and MoS<sub>2</sub>-TFN membranes, which has good prospects in water desalination, the performance comparison were shown in Table S3.

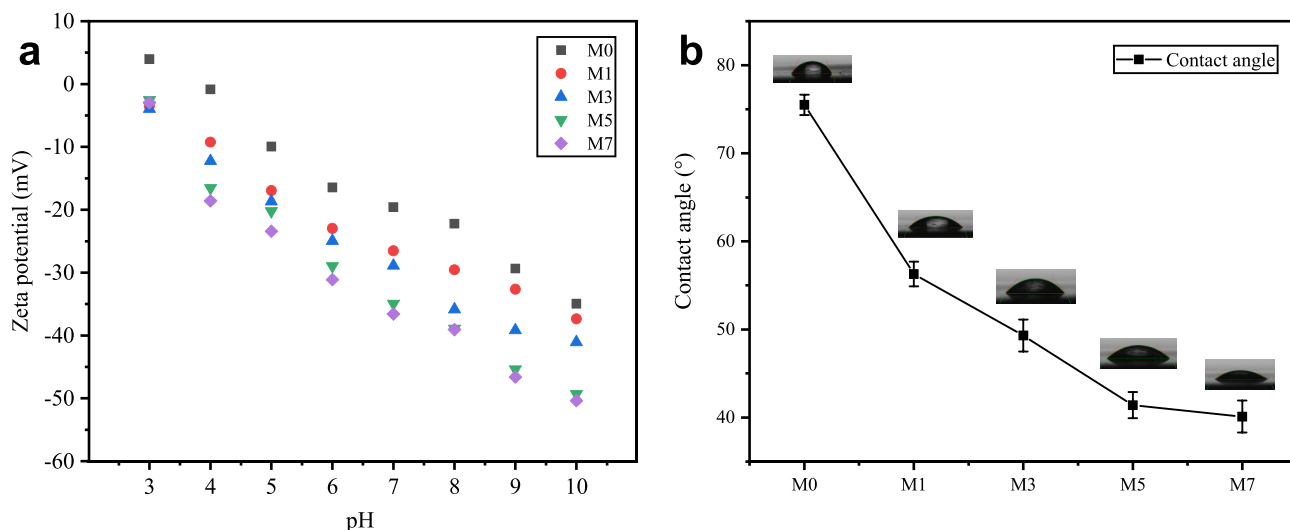


Fig. 10. Zeta potential (a) and contact angle (b) of NF membranes.

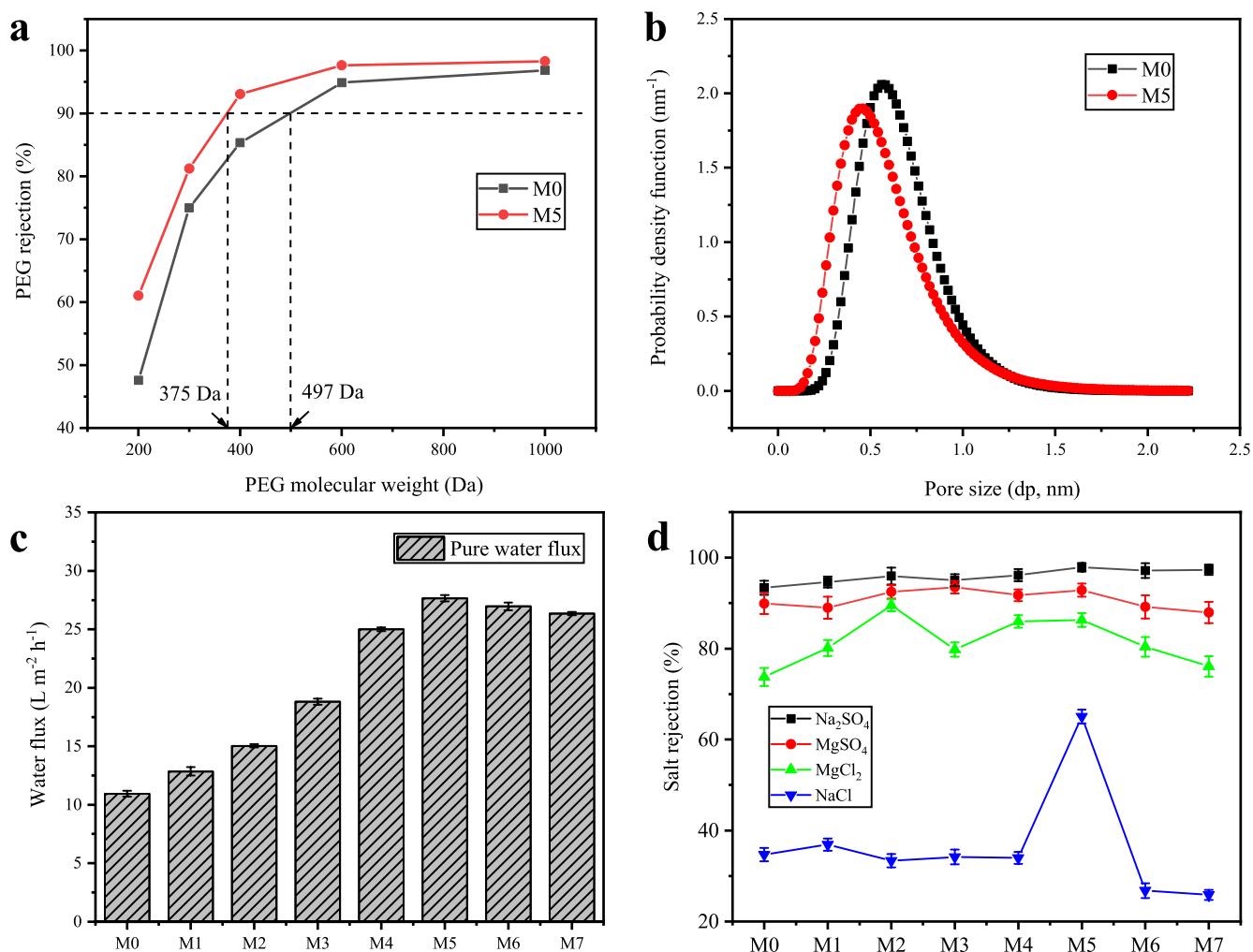


Fig. 11. Molecular weight cut-off (a), pore size and pore size distribution (b) of M0 and M5 membranes, pure water flux (c) and salt rejection (d).

### 3.4. Antifouling performance of O-MoS<sub>2</sub> NF membrane

BSA as a typical foulant was selected for the membranes fouling characterization. The M0 and M5 were tested three cycles with 500 ppm

BSA solution at pH of 6.0. The normalized water flux of the M0 and M5 were shown in Fig. 12. After 60 min of DI water filtration, the flux of M0 and M5 maintained a stable value. Subsequently, membranes were fouled by BSA solution for 90 min. Normalized water flux of M0

decreased from 1.0 to 0.57 observably when exposed to BSA solution, while flux decline ratio of M5 was smaller than M0, only reduced from 1.0 to 0.78. The water flux of M0 and M5 recovered different after washed by DI water. After three cycles of contamination and cleaning, the FRR of M0 and M5 recovered to 71.9% and 90.4%, respectively. The problem of membrane fouling was related to the hydrophobic interaction, hydrogen bonding, electrostatic repulsion and van der Waals interaction between the membrane surface and the contaminants [77, 78]. The remarkable improvement of the antifouling performance of the M5 membrane could be attributed to the following two aspects: 1) Due to the good hydrophilicity of O-MoS<sub>2</sub>, the TFN membrane hydrophilicity increased, consequently enhanced the antifouling performance [31]. 2) Since both the membrane surface and BSA (pH: 6.0 > pI: 4.7) were negatively charged, therefore, the electrostatic repulsion between the membrane and BSA would have great benefits for the fouling control of the membrane [79]. Therefore, nanosheets with a negative charge and excellent hydrophilicity are considered to effectively improve the antifouling property of TFN membranes.

### 3.5. Stability test of O-MoS<sub>2</sub> NF membrane

For the stability test, M0 and M5 membranes were filtered with a feed solution of 2000 ppm Na<sub>2</sub>SO<sub>4</sub> at a pressure of 3.5 bar, collected permeation at every 30 min and tested salt rejection. The results of M0 and M5 were compared in Fig. 13. The pristine M0 membrane without O-MoS<sub>2</sub> modification showed an approximately 23.2% reduction of water flux during the entire operation. The salt rejection of M0 membrane kept increasing due to the physical compaction of polymeric membrane but maintained stable after 4 h operation. By contrast, M5 membrane showed only a few decrease of water permeation (6.6%) and an extremely stable solute rejection behavior. It indicated that the membrane with O-MoS<sub>2</sub> incorporation exhibited a higher hydraulic pressure resistance compared with the pristine membrane. This could be ascribed to the robust 2D nanosheets endowed the cross-linked polyamide layer with higher mechanical strength. In addition, the membranes prepared via coating of 2D nanosheets or layer-by-layer assembling techniques are generally unstable in the long-term filtration because of the peel off of the coating layer. However, the in-situ incorporation of O-MoS<sub>2</sub> in the polyamide selective layer via interfacial polymerization could effectively address this issue. The O-MoS<sub>2</sub> modified TFN NF membrane with high water desalination performance, coupled with good stability has demonstrated to be promising in industrial application.

## 4. Conclusion

The synthesized O-MoS<sub>2</sub> showed higher hydrophilicity and higher electronegativity because of the strong oxidation process, leading to a more oxygen charged surfaces. The incorporation the O-MoS<sub>2</sub> in the polyamide matrix endowed the membrane surface with improved hydrophilicity, surface roughness and negative charge. The PEG filtration experiment demonstrated that the membrane had a decreased mean effective pore diameter from 0.65 to 0.56 nm. As consequences, the 0.010 wt/v% O-MoS<sub>2</sub> TFN membrane showed the optimal water flux of 27.7 L m<sup>-2</sup> h<sup>-1</sup>, which was 2.5 times than the compared with the control 10.9 L m<sup>-2</sup> h<sup>-1</sup>. The rejection of Na<sub>2</sub>SO<sub>4</sub>, MgSO<sub>4</sub>, MgCl<sub>2</sub> and NaCl at 2000 ppm, 3.5 bar, 25 °C was 97.9%, 92.9%, 86.3% and 65.1%, respectively. Antifouling experiments showed that 90.4% of the flux recovery rate was maintained for 0.010 wt/v% TFN membrane under the condition of BSA concentration of 500 ppm, which was a significant improvement compare to the 71.9% of the TFC membrane, showing the excellent antifouling performance. Advanced few-layers 2D O-MoS<sub>2</sub> nanosheets with excellent hydrophilicity and negative charged provide a theoretical basis for designing NF membranes with high selectivity, high permeability and excellent antifouling performance. The O-MoS<sub>2</sub> as a new generation of functional materials is expected to be effectively applied in

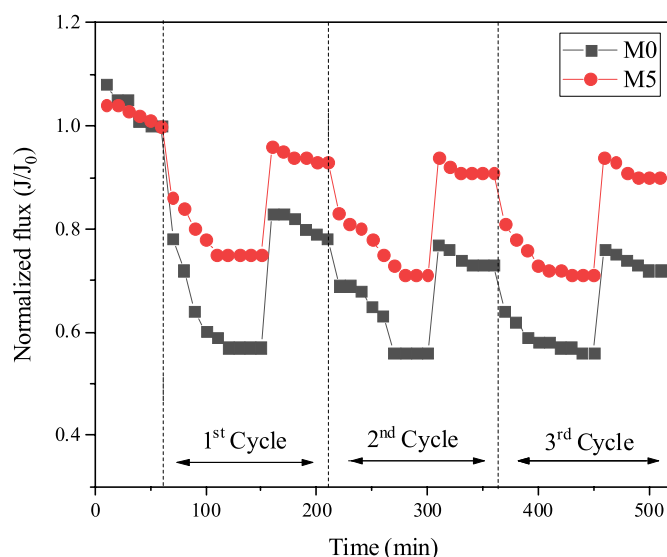


Fig. 12. Antifouling properties of M0 and M5, tested with 500 ppm BSA.

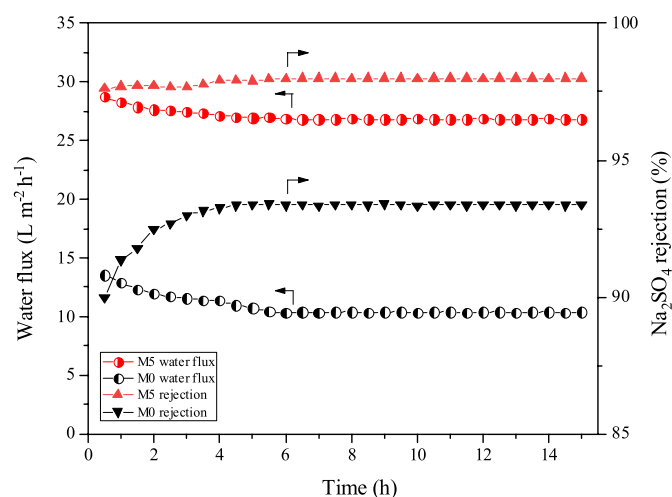


Fig. 13. Stability test of the M0 and M5, 2000 ppm Na<sub>2</sub>SO<sub>4</sub> was used as solute.

water treatment and other fields in the future.

### Declaration of competing interest

There are no conflicts to declare.

### CRediT authorship contribution statement

**Shishi Yang:** Writing - original draft, Investigation, Writing - review & editing. **Qinliang Jiang:** Writing - original draft, Investigation, Writing - review & editing. **Kaisong Zhang:** Conceptualization, Funding acquisition, Formal analysis, Writing - original draft, Investigation, Writing - review & editing.

### Acknowledgements

This work was supported by grants from the National Key R&D Program of China (2018YFC1903205), the Bureau of Frontier Sciences and Education (QYZDB-SSW-DQC044), the Bureau of International Cooperation (132C35KYSB20160018) and the Chinese Academy of Sciences and the Joint Project between CAS-CSIRO (132C35KYSB20170051). The authors thank Hongyun Ren and Zhen Xu

at the Center of Analysis & Measurement from Institute of Urban Environment, CAS for the TEM and XPS measurement, respectively. And the valuable comments from Fang Fang, Xing Wu, Huali Tian and Qin Liu. In particular, Yi Li from the KU Leuven in Belgium gave a lot of advice and help. The authors would like to acknowledge Mrs. Temitope Fausat Ajibade (Nee Otun) for the grammatical revision.

## Appendix A. Supplementary data

Supplementary data to this article can be found online at <https://doi.org/10.1016/j.memsci.2020.118052>.

## References

- [1] D.M. Warsinger, S. Chakraborty, E.W. Tow, M.H. Plumlee, C. Bellona, S. Loutatidou, L. Karimi, A.M. Mikelonis, A. Achilli, A. Ghassemi, L.P. Padhye, S. A. Snyder, S. Curcio, C. Vecitis, H.A. Arafat, J.H.t. Lienhard, A review of polymeric membranes and processes for potable water reuse, *Prog. Polym. Sci.* 81 (2016) 209–237.
- [2] Y.-F. Mi, F.-Y. Zhao, Y.-S. Guo, X.-D. Weng, C.-C. Ye, Q.-F. An, Constructing zwitterionic surface of nanofiltration membrane for high flux and antifouling performance, *J. Membr. Sci.* 541 (2017) 29–38.
- [3] G.M. Geise, H.B. Park, A.C. Sagle, B.D. Freeman, J.E. McGrath, Water permeability and water/salt selectivity tradeoff in polymers for desalination, *J. Membr. Sci.* 369 (2011) 130–138.
- [4] X.-L. Wang, W.-J. Shang, D.-X. Wang, L. Wu, C.-H. Tu, Characterization and applications of nanofiltration membranes: state of the art, *Desalination* 236 (2009) 316–326.
- [5] J. Hu, Z. Lv, Y. Xu, X. Zhang, L. Wang, Fabrication of a high-flux sulfonated polyamide nanofiltration membrane: experimental and dissipative particle dynamics studies, *J. Membr. Sci.* 505 (2016) 119–129.
- [6] M. Paul, S.D. Jons, Chemistry and fabrication of polymeric nanofiltration membranes: a review, *Polymer* 103 (2016) 417–456.
- [7] P. Xu, J.E. Drewes, T.-U. Kim, C. Bellona, G. Amy, Effect of membrane fouling on transport of organic contaminants in NF/RO membrane applications, *J. Membr. Sci.* 279 (2006) 165–175.
- [8] J.H. Jhaveri, Z.V.P. Murthy, A comprehensive review on anti-fouling nanocomposite membranes for pressure driven membrane separation processes, *Desalination* 379 (2016) 137–154.
- [9] L. Dong, X. Huang, Z. Wang, Z. Yang, X. Wang, C. Tang, A thin-film nanocomposite nanofiltration membrane prepared on a support with in situ embedded zeolite nanoparticles, *Separ. Purif. Technol.* 166 (2016) 230–239.
- [10] H. Huang, X. Qu, H. Dong, L. Zhang, H. Chen, Role of NaA zeolites in the interfacial polymerization process towards a polyamide nanocomposite reverse osmosis membrane, *RSC Adv.* 3 (2013) 8203–8207.
- [11] H. Wu, B. Tang, P. Wu, Optimizing polyamide thin film composite membrane covalently bonded with modified mesoporous silica nanoparticles, *J. Membr. Sci.* 428 (2013) 341–348.
- [12] M.R.S. Kebria, M. Jahanshahi, A. Rahimpour, SiO<sub>2</sub> modified polyethyleneimine-based nanofiltration membranes for dye removal from aqueous and organic solutions, *Desalination* 367 (2015) 255–264.
- [13] B. Rajaeian, A. Rahimpour, M.O. Tade, S. Liu, Fabrication and characterization of polyamide thin film nanocomposite (TFN) nanofiltration membrane impregnated with TiO<sub>2</sub> nanoparticles, *Desalination* 313 (2013) 176–188.
- [14] H.S. Lee, S.J. Im, J.H. Kim, H.J. Kim, J.P. Kim, B.R. Min, Polyamide thin-film nanofiltration membranes containing TiO<sub>2</sub> nanoparticles, *Desalination* 219 (2008) 48–56.
- [15] Z.-X. Low, J. Ji, D. Blumenstock, Y.-M. Chew, D. Wolverson, D. Mattia, Fouling resistant 2D boron nitride nanosheet – PES nanofiltration membranes, *J. Membr. Sci.* 563 (2018) 949–956.
- [16] H. Gao, Q. Shi, D. Rao, Y. Zhang, J. Su, Y. Liu, Y. Wang, K. Deng, R. Lu, Rational design and strain engineering of nanoporous boron nitride nanosheet membranes for water desalination, *J. Phys. Chem. C* 121 (2017) 22105–22113.
- [17] J. Yu, Y. Zhang, J. Chen, L. Cui, W. Jing, Solvothermal-induced assembly of 2D-2D rGO-TiO<sub>2</sub> nanocomposite for the construction of nanochannel membrane, *J. Membr. Sci.* 600 (2020) 117870.
- [18] F. Fei, L. Cseri, G. Szekely, C.F. Blanford, Robust covalently cross-linked polybenzimidazole/graphene oxide membranes for high-flux organic solvent nanofiltration, *ACS Appl. Mater. Interfaces* 10 (2018) 16140–16147.
- [19] L. Sarango, L. Paseta, M. Navarro, B. Zornoza, J. Coronas, Controlled deposition of MOFs by dip-coating in thin film nanocomposite membranes for organic solvent nanofiltration, *J. Ind. Eng. Chem.* 59 (2018) 8–16.
- [20] Y. Li, L.H. Wee, A. Volodin, J.A. Martensa, I.F.J. Vankelecom, Polymer supported ZIF-8 membranes prepared via an interfacial synthesis method, *Chem. Commun.* 51 (2015) 918–920.
- [21] L. Wang, M. Fang, J. Liu, J. He, L. Deng, J. Li, J. Lei, The influence of dispersed phases on polyamide/ZIF-8 nanofiltration membranes for dye removal from water, *RSC Adv.* 5 (2015) 50942–50954.
- [22] T. Ishigami, K. Amano, A. Fujii, Y. Ohmukai, E. Kamio, T. Maruyama, H. Matsuyama, Fouling reduction of reverse osmosis membrane by surface modification via layer-by-layer assembly, *Separ. Purif. Technol.* 99 (2012) 1–7.
- [23] D. Rana, Y. Kim, T. Matsuura, H.A. Arafat, Development of antifouling thin-film-composite membranes for seawater desalination, *J. Membr. Sci.* 367 (2011) 110–118.
- [24] B.D. McCloskey, H.B. Park, H. Ju, B.W. Rowe, D.J. Miller, B.J. Chun, K. Kin, B. D. Freeman, Influence of polydopamine deposition conditions on pure water flux and foulant adhesion resistance of reverse osmosis, ultrafiltration, and microfiltration membranes, *Polymer* 51 (2010) 3472–3485.
- [25] R. Yang, J. Xu, G. Ozaydin-Ince, S.Y. Wong, K.K. Gleason, Surface-tethered zwitterionic ultrathin antifouling coatings on reverse osmosis membranes by initiated chemical vapor deposition, *Chem. Mater.* 23 (2011) 1263–1272.
- [26] Y. Li, S. Yang, K. Zhang, B.V.d. Bruggen, Thin film nanocomposite reverse osmosis membrane modified by two dimensional laminar MoS<sub>2</sub> with improved desalination performance and fouling-resistant characteristics, *Desalination* 454 (2019) 48–58.
- [27] H. Dong, L. Wu, L. Zhang, H. Chen, C. Gao, Clay nanosheets as charged filler materials for high-performance and fouling-resistant thin film nanocomposite membranes, *J. Membr. Sci.* 494 (2015) 92–103.
- [28] S.-M. Xue, C.-H. Ji, Z.-L. Xu, Y.-J. Tang, R.-H. Li, Chlorine resistant TFN nanofiltration membrane incorporated with octadecylamine-grafted GO and fluorine-containing monomer, *J. Membr. Sci.* 545 (2018) 185–195.
- [29] G. Liu, W. Jin, N. Xu, Graphene-based membranes, *Chem. Soc. Rev.* 44 (2015) 5016–5030.
- [30] J. Zhou, Z. Qin, Y. Lu, X. Li, Q. An, S. Ji, N. Wang, H. Guo, MoS<sub>2</sub>/polyelectrolytes hybrid nanofiltration (NF) membranes with enhanced permselectivity, *J. Taiwan Inst. Chem. Eng.* 84 (2018) 196–202.
- [31] M.S.S.A. Saraswathi, D. Rana, P. Vijayakumar, S. Alwarappan, A. Nagendran, Tailored PVDF nanocomposite membranes using exfoliated MoS<sub>2</sub> nanosheets for improved permeation and antifouling performance, *New J. Chem.* 41 (2017) 14315–14324.
- [32] W. Li, Y. Yang, J.K. Weber, G. Zhang, R. Zhou, Tunable, strain-controlled nanoporous MoS<sub>2</sub> filter for water desalination, *ACS Nano* 10 (2016) 1829–1835.
- [33] M. Heiraniyan, A.B. Farimani, N.R. Aluru, Water desalination with a single-layer MoS<sub>2</sub> nanopore, *Nat. Commun.* 6 (2015) 8616.
- [34] S. Yang, K. Zhang, Few-layers MoS<sub>2</sub> nanosheets modified thin film composite nanofiltration membranes with improved separation performance, *J. Membr. Sci.* (2019) 117526.
- [35] M. Amini, S.A.A. Ramazani, M. Faghihi, S. Fattahpour, Preparation of nanostructured and nanosheets of MoS<sub>2</sub> oxide using oxidation method, *Ultrason. Sonochem.* 39 (2017) 188–196.
- [36] M. Liu, S. Yu, M. Qi, Q. Pan, C. Gao, Impact of manufacture technique on seawater desalination performance of thin-film composite polyamide-urethane reverse osmosis membranes and their spiral wound elements, *J. Membr. Sci.* 348 (2010) 268–276.
- [37] A. Rudawska, E. Jacniacka, Analysis for determining surface free energy uncertainty by the Owen–Wendt method, *Int. J. Adhesion Adhes.* 29 (2009) 451–457.
- [38] X. Wang, H. Zhao, Y. Cao, Y. Su, H. Hui, J. Shen, Surface free energy and microstructure dependent environmental stability of sol-gel SiO<sub>2</sub> antireflective coatings: effect of combined vapor phase surface treatment, *J. Colloid Interface Sci.* 555 (2019) 124–131.
- [39] Y. Li, E. Wong, Z. Mai, B. Van der Bruggen, Fabrication of composite polyamide/Kevlar aramid nanofiber nanofiltration membranes with high permselectivity in water desalination, *J. Membr. Sci.* 592 (2019) 117396.
- [40] Y. Li, E. Wong, A. Volodine, C.V. Haesendonck, K. Zhang, B.V.d. Bruggen, Nanofibrous hydrogel composite membranes with ultrafast transport performance for molecular separation in organic solvents, *J. Mater. Chem.* 7 (2019) 19269–19279.
- [41] J.N. Coleman, M. Lotya, A. O'Neill, S.D.B.e. al, Two-dimensional nanosheets produced by liquid exfoliation of layered materials, *Science* 331 (2011) 568–571.
- [42] J. Drelich, E. Chibowski, D.D. Meng, K. Terpilowski, Hydrophilic and superhydrophilic surfaces and materials, *Soft Matter* 7 (2011) 9804.
- [43] J. Kibsgaard, Z. Chen, B.N. Reinecke, T.F. Jaramillo, Engineering the surface structure of MoS<sub>2</sub> to preferentially expose active edge sites for electrocatalysis, *Nat. Mater.* 11 (2012) 963–969.
- [44] Q. Jiang, H. Tian, K. Zhang, Enhanced performance of poly(m-phenylene isophthalamide) (PMIA) composite hollow fiber ultrafiltration membranes by O-MoS<sub>2</sub> nanosheets modification, *Desalination Water Treat.* 166 (2019) 245–258.
- [45] M.R. Gao, M.K. Chan, Y. Sun, Edge-terminated molybdenum disulfide with a 9.4-Å interlayer spacing for electrochemical hydrogen production, *Nat. Commun.* 6 (2015) 7493.
- [46] Q. Xia, Q. Tan, Tubular hierarchical structure composed of O-doped ultrathin MoS<sub>2</sub> nanosheets grown on carbon microtubes with enhanced lithium ion storage properties, *J. Alloys Compd.* 779 (2019) 156–166.
- [47] C. Guo, X. Guo, W. Chu, N. Jiang, H. Li, FTIR-ATR study for adsorption of trypsin in aqueous environment on bare and TiO<sub>2</sub> coated ZnSe surfaces, *Chin. Chem. Lett.* 31 (2020) 150–154.
- [48] J. Xie, J. Zhang, S. Li, F. Grote, X. Zhang, H. Zhang, R. Wang, Y. Lei, B. Pan, Y. Xie, Controllable disorder engineering in oxygen-incorporated MoS<sub>2</sub> ultrathin nanosheets for efficient hydrogen evolution, *J. Am. Chem. Soc.* 135 (2013) 17881–17888.
- [49] A. Klechikov, J. Yu, D. Thomas, T. Sharifi, A.V. Talyzin, Structure of graphene oxide membranes in solvents and solutions, *Nanoscale* 7 (2015) 15374–15384.
- [50] J. Yin, G. Zhu, B. Deng, Graphene oxide (GO) enhanced polyamide (PA) thin-film nanocomposite (TFN) membrane for water purification, *Desalination* 379 (2016) 93–101.

- [51] P. Thangasamy, S. Oh, S. Nam, I.-K. Oh, Rose-like MoS<sub>2</sub> nanostructures with a large interlayer spacing of ~9.9 Å and exfoliated WS<sub>2</sub> nanosheets supported on carbon nanotubes for hydrogen evolution reaction, *Carbon* 158 (2020) 216–225.
- [52] A.R. Kumarasinghe, L. Samaranayake, F. Bondino, E. Magnano, N. Kottegoda, E. Carlino, U.N. Ratnayake, A.A.P. de Alwis, V. Karunaratne, G.A.J. Amaratunga, Self-assembled multilayer graphene oxide membrane and carbon nanotubes synthesized using a rare form of natural graphite, *J. Phys. Chem. C* 117 (2013) 9507–9519.
- [53] Z. Tan, S. Chen, X. Peng, L. Zhang, C. Gao, Polyamide membranes with nanoscale Turing structures for water purification, *Science* 360 (2018) 518–521.
- [54] A.A. Aziz, K.C. Wong, P.S. Goh, A.F. Ismail, I.W. Azelee, Tailoring the surface properties of carbon nitride incorporated thin film nanocomposite membrane for forward osmosis desalination, *J. Water Process Eng.* 33 (2020) 101005.
- [55] N. Ghaemi, P. Safari, Nano-porous SAPO-34 enhanced thin-film nanocomposite polymeric membrane: simultaneously high water permeation and complete removal of cationic/anionic dyes from water, *J. Hazard Mater.* 358 (2018) 376–388.
- [56] Y. Liu, X. Wang, X. Gao, J. Zheng, J. Wang, A. Volodin, Y.F. Xie, X. Huang, B. Van der Bruggen, J. Zhu, High-performance thin film nanocomposite membranes enabled by nanomaterials with different dimensions for nanofiltration, *J. Membr. Sci.* 596 (2020) 117717.
- [57] S. Khakpour, Y. Jafarzadeh, R. Yegani, Incorporation of graphene oxide/nanodiamond nanocomposite into PVC ultrafiltration membranes, *Chem. Eng. Res. Des.* 152 (2019) 60–70.
- [58] L. Yan, Y. Li, C. Xiang, S. Xianda, Effect of nano-sized Al<sub>2</sub>O<sub>3</sub>-particle addition on PVDF ultrafiltration membrane performance, *J. Membr. Sci.* 276 (2006) 162–167.
- [59] Y. Zhao, Z. Xu, M. Shan, C. Min, B. Zhou, Y. Li, B. Li, L. Liu, X. Qian, Effect of graphite oxide and multi-walled carbon nanotubes on the microstructure and performance of PVDF membranes, *Separ. Purif. Technol.* 103 (2013) 78–83.
- [60] S. Karan, Z. Jiang, A.G. Livingston, Sub-10 nm polyamide nanofilms with ultrafast solvent transport for molecular separation, *Science* 348 (2015) 1347–1351.
- [61] S. Abdikhebari, W. Lei, L.F. Dumée, A.J. Barlow, K. Baskaran, Novel thin film nanocomposite membranes decorated with few-layered boron nitride nanosheets for simultaneously enhanced water flux and organic fouling resistance, *Appl. Surf. Sci.* 488 (2019) 565–577.
- [62] M. Ma, C. Zhang, C. Zhu, S. Huang, J. Yang, Z. Xu, Nanocomposite membranes embedded with functionalized MoS<sub>2</sub> nanosheets for enhanced interfacial compatibility and nanofiltration performance, *J. Membr. Sci.* 591 (2019) 117316.
- [63] R. Ploeger, S. Musso, O. Chiantore, Contact angle measurements to determine the rate of surface oxidation of artists' alkyd paints during accelerated photo-ageing, *Prog. Org. Coating* 65 (2009) 77–83.
- [64] R.N. Wenzel, Resistance of solid surfaces to wetting by water, *Ind. Eng. Chem.* 28 (1936) 988–994.
- [65] Y. Kang, M. Obaid, J. Jang, I.S. Kim, Sulfonated graphene oxide incorporated thin film nanocomposite nanofiltration membrane to enhance permeation and antifouling properties, *Desalination* 470 (2019) 114125.
- [66] Q. Xie, W. Shao, S. Zhang, Z. Hong, Q. Wang, B. Zeng, Enhancing the performance of thin-film nanocomposite nanofiltration membranes using MAH-modified GO nanosheets, *RSC Adv.* 7 (2017) 54898–54910.
- [67] B. Tansel, J. Sager, T. Rector, J. Garland, R.F. Strayer, L. Levine, M. Roberts, M. Hummerick, J. Bauer, Significance of hydrated radius and hydration shells on ionic permeability during nanofiltration in dead end and cross flow modes, *Separ. Purif. Technol.* 51 (2006) 40–47.
- [68] H.-R. Chae, J. Lee, C.-H. Lee, I.-C. Kim, P.-K. Park, Graphene oxide-embedded thin-film composite reverse osmosis membrane with high flux, anti-biofouling, and chlorine resistance, *J. Membr. Sci.* 483 (2015) 128–135.
- [69] J.R. Álvarez, R.A. Peralta, J. Balmaseda, E. González-Zamora, I.A. Ibarra, Water adsorption properties of a Sc(III) porous coordination polymer for CO<sub>2</sub> capture applications, *Inorg. Chem. Front.* 2 (2015) 1080–1084.
- [70] V. Vatanpour, S.S. Madaeni, R. Moradian, S. Zinadini, B. Astinchap, Fabrication and characterization of novel antifouling nanofiltration membrane prepared from oxidized multiwalled carbon nanotube/polyethersulfone nanocomposite, *J. Membr. Sci.* 375 (2011) 284–294.
- [71] Y.-J. Tang, Z.-L. Xu, S.-M. Xue, Y.-M. Wei, H. Yang, Tailoring the polyester/polyamide backbone stiffness for the fabrication of high performance nanofiltration membrane, *J. Membr. Sci.* 541 (2017) 483–491.
- [72] J. Wang, H. Yang, M. Wu, X. Zhang, Z. Xu, Nanofiltration membranes with cellulose nanocrystals as an interlayer for unprecedented performance, *J. Mater. Chem.* 5 (2017) 16289–16295.
- [73] Z. Wang, Z. Wang, S. Lin, H. Jin, S. Gao, Y. Zhu, J. Jin, Nanoparticle-templated nanofiltration membranes for ultrahigh performance desalination, *Nat. Commun.* 9 (2018) 2004.
- [74] L.M. Jin, S.L. Yu, W.X. Shi, X.S. Yi, N. Sun, Y.L. Ge, C. Ma, Synthesis of a novel composite nanofiltration membrane incorporated SiO<sub>2</sub> nanoparticles for oily wastewater desalination, *Polymer* 53 (2012) 5295–5303.
- [75] P. Zhang, J.-L. Gong, G.-M. Zeng, B. Song, W. Cao, H.-Y. Liu, S.-Y. Huan, P. Peng, Novel “loose” GO/MoS<sub>2</sub> composites membranes with enhanced permeability for effective salts and dyes rejection at low pressure, *J. Membr. Sci.* 574 (2019) 112–123.
- [76] X. Liang, P. Wang, J. Wang, Y. Zhang, W. Wu, J. Liu, B. Van der Bruggen, Zwitterionic functionalized MoS<sub>2</sub> nanosheets for a novel composite membrane with effective salt/dye separation performance, *J. Membr. Sci.* 573 (2019) 270–279.
- [77] F. Yan, H. Chen, Y. Lü, Z. Lü, S. Yu, M. Liu, C. Gao, Improving the water permeability and antifouling property of thin-film composite polyamide nanofiltration membrane by modifying the active layer with triethanolamine, *J. Membr. Sci.* 513 (2016) 108–116.
- [78] C.Y. Tang, T.H. Chong, A.G. Fane, Colloidal interactions and fouling of NF and RO membranes: a review, *Adv. Colloid Interface Sci.* 164 (2011) 126–143.
- [79] A.E. Childress, M. Elimelech, Effect of solution chemistry on the surface charge of polymeric reverse osmosis and nanofiltration membranes, *J. Membr. Sci.* 119 (1996) 253–268.